Origin of Axial and Radial Expansions in Carbon Nanotubes Revealed by Ultrafast Diffraction and Spectroscopy

Giovanni M. Vanacore, Renske M. van der Veen,[†] and Ahmed H. Zewail*

Physical Biology Center for Ultrafast Science and Technology, Arthur Amos Noyes Laboratory of Chemical Physics, California Institute of Technology, Pasadena, California 91125, United States. [†]Present address: Max Planck Institute for Biophysical Chemistry, Göttingen (Germany), and the Deutsches Elektronen Synchrotron (DESY), Hamburg (Germany).

ABSTRACT The coupling between electronic and nuclear degrees of freedom in low-dimensional, nanoscale systems plays a fundamental role in shaping many of their properties. Here, we report the disentanglement of axial and radial expansions of carbon nanotubes, and the direct role of electronic and vibrational excitations in determining such expansions. With subpicosecond and subpicometer resolutions, structural dynamics were explored by monitoring changes of the electron diffraction following an ultrafast optical excitation, whereas the transient behavior of the charge distribution was probed by time-resolved, electron-energy-loss spectroscopy. Our experimental results, and supporting density functional theory calculations, indicate that a population of the excited carriers in the antibonding orbitals of the nanotube walls drives a transient axial deformation in ~1 ps; this deformation relaxes on a much longer time scale, 17 ps, by nonradiative decay. The electron-driven expansion is distinct from the phonon-driven dynamics observed along the radial direction, using the characteristic Bragg reflections; it occurs in 5 ps. These findings reveal the nonequilibrium distortion of the unit cell at early times and the role of the electron(phonon)-induced stress in the lattice dynamics of one-dimensional nanostructures.

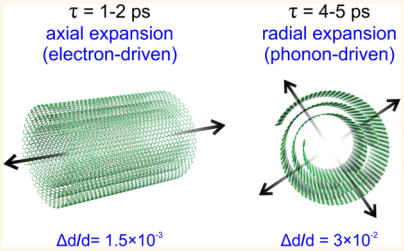

KEYWORDS: carbon nanotubes · structural dynamics · 4D electron microscopy · ultrafast electron diffraction · femtosecond electron-energy-loss spectroscopy

The interaction between electrons and the lattice is at the origin of a variety of phenomena in the condensed phase, and it is fundamental for transport and optical properties.[1−5] Carbon nanotubes are one-dimensional nanostructures, whose remarkable properties[6,7] make them promising building-blocks for the design of a new generation of nano- and optoelectronic devices.[8−11] Because of their peculiar electronic and atomic structures, they are considered as prototypical systems to investigate electron−lattice interaction at the nanoscale. However, despite the continued interest and the *plethora* of studies on the subject, understanding of the underlying processes remains the subject of many studies.[3−5,12−16] For example, the extent of spatial localization and charge-carriers delocalization in correlation with the deformation of the unit cell in the nonequilibrium regime, which are important to the efficacy of electron mobility[17] and electric conduction,[18] are still in need of further investigation.

Optical reflection,[19,20] Raman spectroscopy[21−23] and photoemission[13,24] studies have provided valuable insights into the initial electronic processes and dynamics of optical phonons in carbon nanotubes. However, because of selection rules, optical methods excite the system only to the center of the Brillouin zone (Γ region), where momentum conservation is fulfilled, thus limiting the information on the (acoustic) phonons excited toward the zone boundaries. Moreover, although variations of Raman frequencies might provide some information on lattice deformation,[25] when the dynamics evolves out of the equilibrium state and is not driven by the phonon excitation, it becomes challenging to obtain structural changes directly, because the Raman response to the optical excitation is determined by an intricate interplay of many factors.[22,25] When observed with atomic-scale spatial and femtosecond temporal resolutions, the nonequilibrium structural changes and relaxations can be directly

* Address correspondence to zewail@caltech.edu.

Received for review November 16, 2014 and accepted January 28, 2015.

Published online January 30, 2015
10.1021/nn506524c

studied in the nanoscale systems. It is worth noting that the wavelength used in optical probing far exceeds the interatomic distances, rendering complete structural determination very challenging. Time-resolved diffraction, using ultrashort electrons or X-ray pulses, whose wavelengths are in the scale of picometers and angstrom, respectively, provides the means for the direct probing of structural dynamics, and it has been successfully applied in numerous nanoscale systems.[26−33]

Here, we investigate the lattice and charge distribution dynamics in carbon nanotubes by employing ultrafast electron crystallography (UEC) and femtosecond electron-energy-loss spectroscopy (FEELS). By measuring the temporal changes of the electron diffraction for multiwalled tubes we monitored the lattice evolution along the radial and axial directions. Additionally, the accompanying transient change of the charge distribution was examined through FEELS in single-walled tubes. We found that a population of carriers in the antibonding orbitals of the nanotube walls leads to a nonequilibrium lattice deformation along the tube axis on a time scale of ~1 ps mediated by C−C bond weakening, whereas along the radial direction the structural dynamics is driven by the excitation of (acoustic) phonons in 5 ps. The approach described here represents a unique methodology for the unraveling of electronic- and vibrational-induced changes of the unit cell in nanostructured materials. Also, to date, this is the first direct visualization of electron-driven ultrafast bond dilatation reported for carbon nanotubes.

RESULTS AND DISCUSSION

The experimental UEC description is given in the Experimental Section. Briefly, ultrashort electron pulses are focused on the sample in a normal incidence, and diffraction is performed in the transmission geometry. The dynamics are initiated by laser pulses at 800 nm (120 fs, 1 kHz), and the diffracted electrons are probed at different delay times between the optical and the electron pulses. The multiwalled carbon nanotubes were prepared according to the procedure reported in previous works[34,35] and described in the Experimental Section.

From the electron microscopy images (see Figure 1a), we determine their diameter to vary between 10 and 20 nm. Several studies[36−40] have shown that the energetically stable structure for multiwalled tubes with external diameter larger than 10 nm is a mixture of a "Russian-doll" structure (closed concentric tubes) and a "scroll" structure (rolled-up graphene sheets). The preservation of helicity, rather than the utilization of van der Waals forces, represents the organizing principle for the tubes, making this hybrid structure most likely to form under common synthesis conditions.[39] Nevertheless, it is important to stress that the atomic structure within the nanotube walls is not affected by their particular interplanar arrangement.

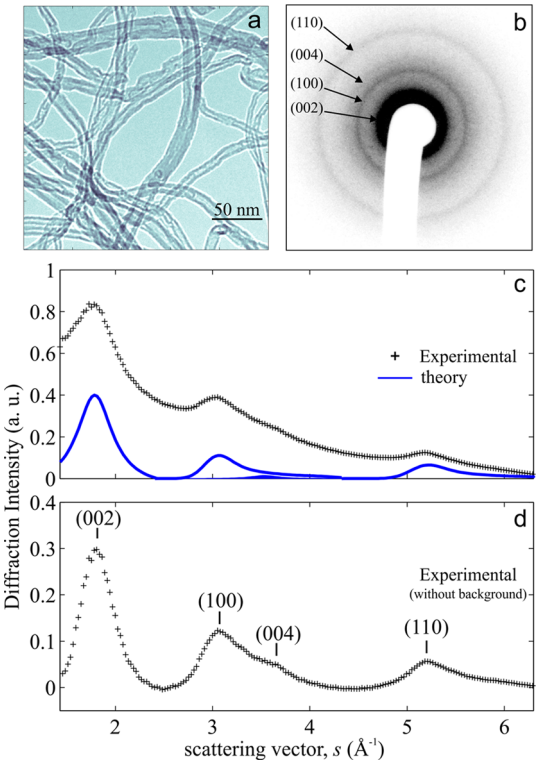

Figure 1. Morphology and diffraction. (a) Representative electron microscopy image of the investigated multiwalled carbon nanotubes. (b) Debye−Scherrer diffraction pattern of the nanotubes network. (c) Experimentally measured (black +) and theoretical profiles (blue solid curves) of the diffraction intensity as a function of the scattering vector, s (rocking curve). (d) Experimental rocking curve after subtraction of an inverse polynomial background. The (00*l*) and (*hk*0) reflections are associated with the radial (interplane) and axial (in-plane) directions, respectively.

The diffraction pattern, shown in Figure 1b, consists of Debye−Scherrer rings since the sample is a network of randomly oriented tubes. After azimuthally averaging the ring pattern (see Figure 1c−d), the peaks are indexed on the basis of hexagonal graphite: (00*l*) and (*hk*0) reflections are associated with radial (interplane) and axial (in-plane) directions, respectively (see Experimental Section for more details).

The transient behavior of the Bragg reflections mirrors the lattice dynamics. In kinematic theory, the diffraction intensity, *I*, is proportional to the square modulus of the structure factor, *F*; that is, $I \propto |F|^2$. *F* depends on the displacement of the atoms, $\mathbf{u}_j$, and is given by

$$F = \sum_j \zeta_j \exp[i\mathbf{s}\cdot(\mathbf{R}_j + \mathbf{u}_j(t))] \qquad (1)$$

where $\mathbf{s}$ is the scattering vector, $\mathbf{R}_j$ is the equilibrium position of the *j*th atom, and ζ_j is the atomic scattering factor. Any lattice motion able to change the atomic displacement, like those of optical and acoustic phonons, can cause the diffraction intensity to change. In fact, when phonons are excited, the vibration of atoms around their equilibrium position, which is described

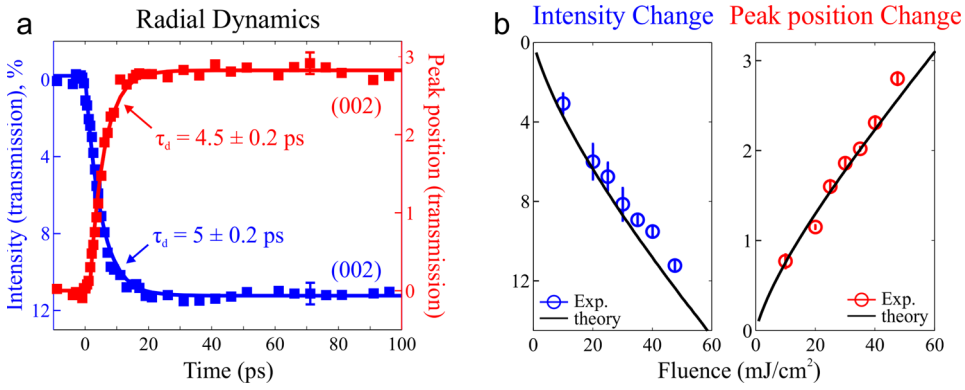

Figure 2. Radial dynamics and diffraction behavior with fluence. (a) Transient evolution of the intensity (blue squares) and peak position (red squares) change for the radial (002) reflection at 48 mJ/cm^2. The solid curves represent the best fit of the experimental data with single-exponential functions. The change of the peak position is defined as $[s_0 - s(t)]/s_0$, where s_0 and s are the peak positions before and after the optical excitation, and is expressed in units of 10^{-2}. This can be directly correlated to the lattice change $[d(t) - d_0]/d_0$, where d is the interatomic distance, along the (002) direction. (b) Experimental (data points) and calculated (solid curves) fluence dependence of the intensity (left panel) and peak position (right panel) measured at long delay times (Δt = 100 ps) for the (002) reflection.

by the mean-square displacement $\langle \mathbf{u}_j^2 \rangle$, leads to a net nonuniform displacement within the lattice, and consequently to the loss of electron interference responsible for the decrease of diffraction intensity. However, a homogeneous deformation (expansion/contraction) of the lattice (i.e., $\mathbf{u}_j$ being independent of j) changes only the phase of the structure factor, such that the intensity is not affected, although it will modify the scattering vector of the Bragg peaks according to the relation: $[s_0 - s(t)]/s_0 = [d(t) - d_0]/d_0$, where d is the interatomic distance and the subscript "0" indicates the corresponding quantities before laser excitation.

The transient behavior of the radial (002) and axial (110) reflections is shown in Figures 2a and 3a, respectively. Similar results are obtained for the (004) and (100) peaks (see Figure S4 in the Supporting Information). For the radial dynamics both the intensity and peak position are characterized by a similar time scale: 5.0 ± 0.2 ps for the intensity, and 4.5 ± 0.2 ps for the peak position. For the axial dynamics, the intensity also evolves in 5.0 ± 0.3 ps, whereas the peak position exhibits an initial faster change followed by a slower recovery before reaching its equilibrium value.

To unravel the nature of the observed dynamics, we first show in Figures 2b and 3b that the intensity and peak position changes at long delay times (Δt = 100 ps) are well interpreted within an equilibrium heating model (see ref 31, and Supporting Information). The thermal motions excited by the pump laser lead to a temperature increase of the lattice. This induces a loss of Bragg interferences which in turn results in a reduction of the diffraction intensity. The reduction is quantitatively described by the Debye–Waller relation,[31] where the energy scale of the thermal motions is defined by the Debye temperature, Θ_D. Using Θ_D^{rad} = 533 K[41] and Θ_D^{ax} = 1930 K[42] for interplane and in-plane thermal vibrations, respectively, we calculated the intensity change at equilibrium for the radial and axial peaks. Their trend as a function of the fluence is shown in Figures 2b and 3b (left panels). A satisfactory agreement with the experimental results is obtained.

Besides the intensity decrease, the thermal heating also induces a lattice expansion, which is due to the anharmonicity of the interatomic potential. The change of the interatomic distance is given by $\Delta d/d_0 = \int_{T_0}^{T_0 + \Delta T} \alpha(T) dT$, where $\alpha(T)$ is the linear expansion coefficient. For the radial direction, $\alpha_{(00l)}$ is 26 × 10^{-6} K^{-1}[36] and the calculated fluence dependence of the expansion, plotted in Figure 2b (right panel), well reproduces the experimental results. For the axial direction, as shown in Figure 3b (right panel), the experimentally measured change lies in between the theoretical curves for graphite[43] and single-walled nanotubes,[44] as expected for a multiwalled hybrid concentric/scrolled morphology. It is worth mentioning that the relative peak position changes measured at equilibrium are similar to those reported by Park *et al.*[35] in a previous publication.

Having established that the observed structural dynamics at long delay times reflect the equilibrium regime, we can now address the transient behavior at early times. The time constant for the radial dynamics (ranging from 4.5 to 5 ps, see Figure 2a) well correlates with the typical time constant for excitation of acoustic phonons in carbon nanotubes: 5.3 ps as calculated by Lazzeri *et al.*,[45] and 4.4 ps as obtained by Dyatlova *et al.*[16] In carbon structures, a rapid internal thermalization of the excited electrons occurs in 100 fs by electron–electron scattering.[46] After the electronic system acquires a Fermi–Dirac distribution, the energy is transferred to strongly coupled optical phonons (SCOPs),[24] which finally decay *via* anharmonic scatterings to low-energy acoustic phonons on a time scale of 4–5 ps.[16,24,45,47]

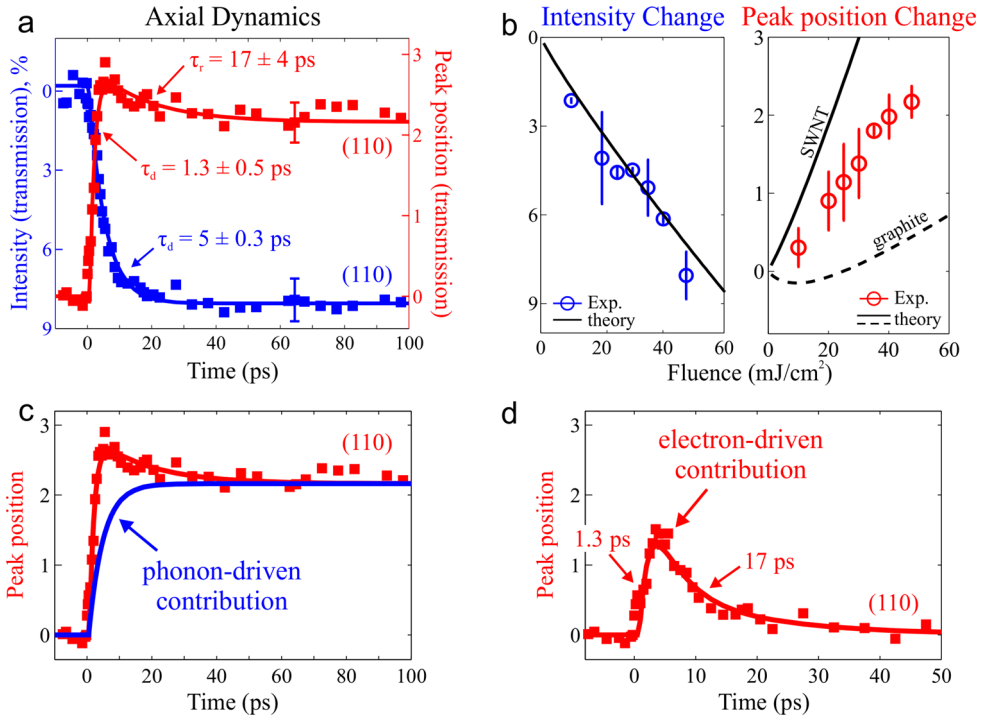

Figure 3. Axial dynamics and diffraction behavior with fluence. (a) Transient evolution of the intensity (blue squares) and peak-position (red squares) changes for the axial (110) reflection at 48 mJ/cm^2. The blue solid curve is the best fit of the data with a single-exponential function, whereas the red solid curve is obtained by the superposition of a fast expansion and a slower recovery, after subtraction of the phonon-driven contribution (see panels c−d). The change of the peak position is defined as $[s_0 - s(t)]/s_0$ and is expressed in units of 10^{-3}. This can be directly correlated to the lattice change along the (110) direction. (b) Experimental (data points) and calculated (solid curves) fluence dependence of the intensity (left panel) and peak position (right panel) measured at long delay times (Δt = 100 ps) for the (110) reflection. (c) The transient change of the peak position is replotted together with a single-exponential rise with a time constant of 5 ps (blue solid curve), which is the phonon-driven contribution to the lattice change. (d) The data set obtained after the subtraction of the phonon-driven contribution highlights the purely electron-driven part; it is fitted with the combination of a fast exponential increase and a slow exponential decay.

For the axial direction, the (apparent) transient change of the intensity occurs in 5.0 ± 0.3 ps and may still be interpreted within the phonon-driven picture described above. However, if the dynamics were only mediated by the excitation of acoustic modes, we should expect the peak position to also change with a time constant of approximately 5 ps, contrary to the experimentally observed behavior (Figure 3a). When the phonon-driven component is subtracted from the peak position change (Figure 3c), the trend shown in Figure 3d is obtained, from which we determine a time constant of 1.3 ± 0.5 ps for the initial change and of 17 ± 4 ps for the final recovery. This behavior cannot be associated with a phonon-driven dynamics, and must be related to nonequilibrium processes that take place within the excited electronic distribution.

The electronic structure of carbon nanotubes comprises a σ band, which has a very large gap, and a π band around the Fermi level.[40,48] Hence, the optical excitation at 1.55 eV promotes electrons from the bonding π to the antibonding π^* states. The interaction with SCOPs causes the population of hot electrons to relax toward the energy minimum of the conduction band at K and K′ points of the Brillouin zone. Theoretical calculations predict an intraband relaxation time for the carriers in multiwalled carbon nanotubes of 1−2 ps,[13,49] which well correlates with the measured time constant of the axial expansion (1.3 ps). On this time scale, a significant portion of the antibonding charge distribution lies in the C−C bonds within the nanotube walls.

The ultrafast axial expansion, or structural deformation, is thus the result of an instantaneous in-plane stress created by the weakening of the interatomic potential due to the antibonding population (see schematics in Figure 5b).[50−54] It is worth noting that this electron-driven change of the C−C bond length creates a homogeneous axial expansion without changing the symmetry of the nanotube lattice. Thus, only the phase of the structure factor F is modified, and therefore, the diffraction intensity, which is proportional to $|F|^2$, is expected to remain unaffected by the electron excitation, but to be altered by the phonon-driven contribution, as experimentally observed (see Figure 3a).

The single-bond picture adopted above is useful to describe the initial ultrafast axial change. However, a proper description of the electronic states must consider the energy bands formed by a linear combination

of π and π^* orbitals over adjacent bond sites. Such bands are important to consider for the final recovery that occurs on a much longer time scale, 17 ps (Figure 3d). Because the diffusion length of conduction electrons traveling along the nanotube walls is of a few micrometers,[55] and the typical separation between defects sites is smaller than 100 nm,[56,57] carriers can be efficiently trapped in the energy states created by defects around the Fermi level.[58] A nonradiative decay, evolving on a time scale of 10−15 ps,[55,59,60] therefore, will relax the electronic distribution from the conduction band toward these trapping sites. On a similar time scale, nonradiative electron−hole recombination, mediated by plasmon emission and Auger scattering,[61] is also likely to occur. These processes lead to the depopulation of the antibonding states and the creation of a new equilibrium charge distribution. The electron-driven stress is thus removed, and the lattice finally relaxes toward the equilibrium deformation.

The correlation between the observed axial structural change and the evolution of the charge distribution can be further examined by monitoring the collective dynamics of valence electrons using FEELS.[62,63] Since we are mainly interested in the transient change occurring within the nanotube walls, the FEELS measurements were performed on single-walled nanotubes (diameter of ∼1 nm; see Experimental Section for details of sample preparation). The FEELS experiments are extensively described in previous works[62,63] and detailed in the Experimental Section. The static EEL spectrum is shown in Figure 4a. The feature at 5.5 eV is the π plasmon, whereas the peak centered at 20 eV is the $\pi+\sigma$ plasmon (due to the collective excitation of all valence electrons).[64] In single-walled nanotubes only tangential modes are excited,[64] and the observed features represent in-plane surface modes polarized along the tube axis.[65,66]

The time dependence of the spectral bands is displayed in Figure 4b as a two-dimensional difference map, where each spectrum is referenced to the averaged one taken before time zero. The strong signal around zero time-delay and zero energy-loss is due to the interaction between the probing electrons and the electric field scattered by the nanotubes.[67] Both the π and $\pi+\sigma$ plasmon bands undergo a red-shift (reduction of the peak energy), which indicates a decrease of the in-plane electron density and thus an expansion of the lattice along the nanotube axis.[68] From the time dependence of the energy position, shown in Figure 4c for the $\pi+\sigma$ plasmon, we obtained a time constant of 0.7 ± 0.2 ps (see Experimental Section for fitting details). This behavior is similar to the axial transients observed in the diffraction data on multiwalled tubes, confirming that the occupation of π^* states results in an overall decrease of the intrawall electron density

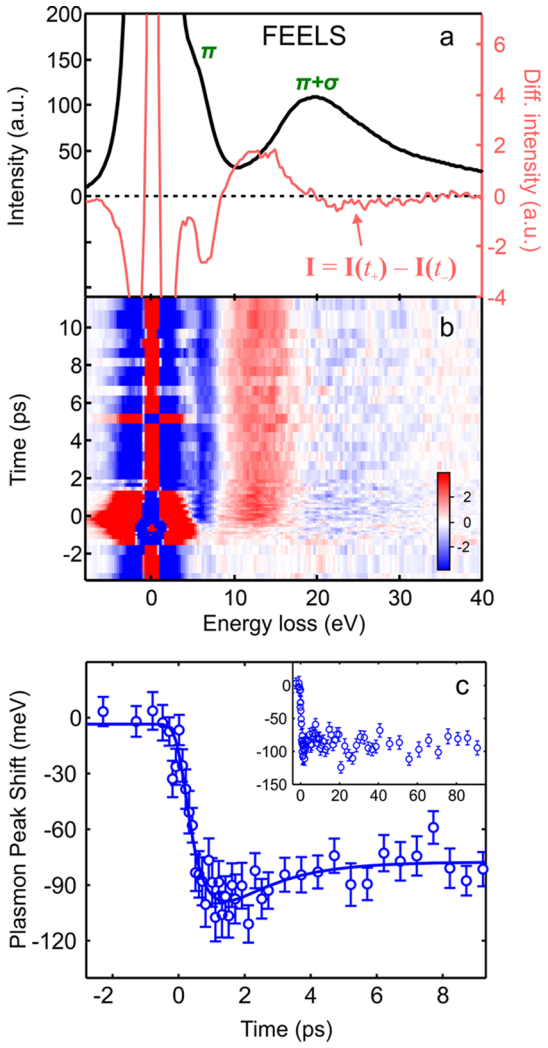

Figure 4. Femtosecond EELS. (a) Static EEL spectrum acquired before excitation (black curve, left axis) in single-walled carbon nanotubes, together with the EEL spectrum taken at 6 ± 2 ps (red curve, right axis) after excitation at λ = 519 nm (20 mJ/cm^2). The π and $\pi+\sigma$ plasmon resonances are labeled. (b) Two-dimensional difference energy-time map referenced to the averaged spectrum taken before zero-time. (c) Time dependence of the energy shift measured for the $\pi+\sigma$ plasmon band. The inset shows the long time scale behavior. We determine a time constant of 0.7 ± 0.2 ps for the initial drop and of 1.6 ± 0.8 ps for the final recovery (see SI for fitting details). The latter value is different from that found in multiwalled nanotubes (17 ps), and is consistent with less defect density in the case of single-walled tubes.

and clearly indicates the general validity of the observed structural dynamics.

To further corroborate our results, we performed *ab initio* calculations, based on the density functional theory (DFT)[69] (details are reported in the Supporting Information). Since we are interested in the change of the bond length within the nanotube walls, the calculations were run for single-walled nanotubes. The electron excitation is simulated by modifying the occupation of the lowest unoccupied (π^*) and highest occupied (π) energy bands. Full structural optimization

of the unit cell is then carried out in order to obtain the change of the C−C bond length.

The calculated lattice expansion along the axial direction for an increasing π^* occupation is shown in Figure 5a. Assuming an excitation of one electron per absorbed photon, we estimate that the effective π^* occupation for a fluence of 48 mJ/cm^2 is about 0.2 electrons per C−C bond, corresponding to a calculated axial expansion of 1.8×10^{-3}. This value is close to the experimental result of 1.5×10^{-3}, as determined from the diffraction data in Figure 3d, after subtracting the phonon-driven contribution. As schematically shown in Figure 5b, a population of the charge carriers in antibonding orbitals induces a significant bond length increase for the C−C bonds within the nanotube walls, which drives the nonequilibrium axial expansion observed experimentally. This is further confirmed by the inspection of the electron density maps (see Figure S2 in the Supporting Information), calculated for two C−C bonds with a π^* occupation of 1e$^-$, as referenced to the ground state (0e$^-$). The map reveals an increase of the electronic charge at the atomic sites, whereas a corresponding depletion is evident in the region of in-between the C atoms.

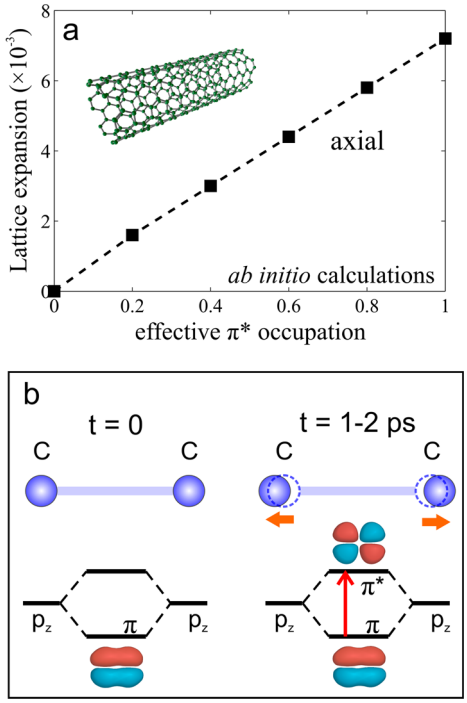

Figure 5. *Ab initio* calculations and orbitals picture. (a) Calculated lattice expansion along the axial direction for a single-walled nanotube as a function of the electron occupation of the π^* antibonding states. The inset represents the nanotube structure used in the calculations. (b) Orbital illustration of the occupation of π^* antibonding states for a C−C bond aligned along the tube axis and the relative effect on its bond length.

CONCLUSION

Ultrafast electron diffraction and energy-loss spectroscopy are reported here for the enabling of the spatiotemporal study of charge distribution and lattice dynamics in carbon nanotubes. As illustrated in Figure 6, the population of the excited carriers in antibonding orbitals of the nanotube walls leads to a nonequilibrium deformation along the tube axis on a time scale of 1−2 ps (Figure 6a), which relaxes with a time constant of 17 ps by nonraditive decay (Figure 6c). This behavior is distinct from the dynamics observed along the radial direction, which is phonon-driven and evolves in 5 ps (Figure 6b). Because ultrafast electron diffraction and energy-loss spectroscopy provide the

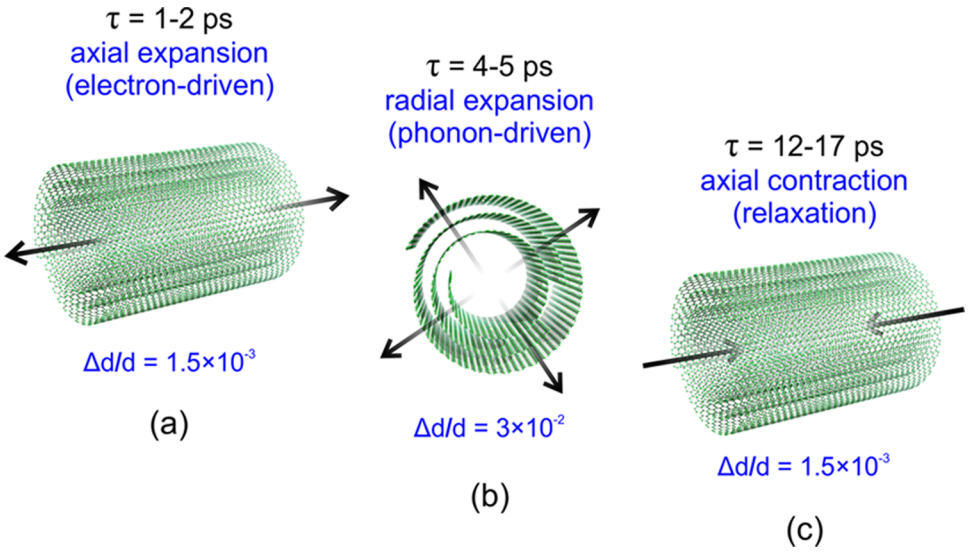

Figure 6. Ultrafast structural evolution. Schematic representation of the structural evolution in multiwalled carbon nanotubes. An electron-driven expansion along the tube axis occurs in 1−2 ps (panel a), which relaxes with a time constant of 12−17 ps (panel c). Along the radial direction, a phonon-driven larger expansion takes place in 4−5 ps (panel b).

suitable temporal and spatial resolutions, this approach should be of general use for unraveling the electronic- and vibrational-induced dynamics in other nanostructured materials.

EXPERIMENTAL SECTION

UEC Experiments. The setup for UEC experiments at Caltech has already been described in details elsewhere.[70] Briefly, electron pulses with energy per particle of 30 keV and subpicosecond pulse width are generated in a photoelectron gun (Kimball Physics, Inc.) after irradiation of a LaB_6 photocathode with 120 fs UV laser pulses (λ = 266 nm). The electron beam is focused in normal incidence on the sample surface. The electron beam diffracted from the sample is recorded in a transmission geometry on a phosphor-screen/MCP/CCD assembly. The dynamics are initiated by femtosecond laser pulses at 800 nm (120 fs, 1 kHz) with a fluence varying between 10 and 48 mJ/cm^2. The fluence of the excitation laser at the sample position was calibrated by scanning a knife edge across the laser profile and recording the passing residual pulse energy. The diffracted electrons are invoked in the stroboscopic mode and for different delay times between the optical pulse and the electron pulse.

The preparation of multiwalled carbon nanotubes (MWNTs) has already been reported in a previous work.[34] Briefly, the nanotubes were grown by chemical vapor deposition (CVD, Aldrich, >90% purity), which represents the most common and widely used synthesis technique because of its potential for their large-scale production.[71] The nanotubes were dispersed in nanopure water containing sodium dodecyl sulfate *via* sonication for several hours. After sonication, the mixture was spun in a centrifuge and the top layer was decanted and separated from the denser portion, which was discarded. A droplet of the decanted mixture was placed onto a 1000-mesh copper grid and then dried out by annealing at 80 °C in N_2 atmosphere for 30 min. In Figure S1 of the Supporting Information we show the Raman spectrum of the investigated multiwalled tubes, which is in good quantitative agreement with those reported in the literature for CVD-grown nanotubes (see Supporting Information for details).

The diffraction pattern consists of Debye−Scherrer rings since the sample is a patch of randomly oriented tubes. The center of the diffraction rings in each pattern was determined by a Hough transform as used in image theory, allowing us to compensate for any drift of the electron beam due to transient electric fields.[72] The movement of the transmitted direct beam was also monitored and exhibited similar behavior as the ring center. Azimuthally averaging of the ring pattern gives the diffraction intensity as a function of the scattering vector, **s** (rocking curve). The peaks are indexed, on the basis of hexagonal graphite, in (00*l*) and (*hk*0) reflections.

For data analysis, the rocking curve is decomposed into a background (inverse polynomial) and diffraction peaks. Gaussian profiles were used for the (002) and (004) peaks. However, an asymmetric line shape must be used for the (100) and (110) peaks, as proposed by Yang *et al.*,[73] because of the turbostratic nature of the multiwalled nanotubes, which is related to the lack of interlayer stacking order.[74] The absence of correlation among the fitted positions of the Bragg peaks is verified by evaluating the covariance matrix, from which a Pearson's coefficient, *p*, of 0.11 is obtained (complete correlation would be present if *p* is 1 or −1).

To ensure that no radiation damage has occurred during the measurements, we monitored the intensity of the (002) and (110) diffraction peaks at zero time-delay as a function of the acquisition time (see Figure S3 in the Supporting Information). No detectable change is observed in both cases, attesting that the same degree of crystallinity is preserved during the measurements made here.

The experimental time dependence of the peak-position change shown in Figures 2 and 3 for the radial (002) and the axial (110) reflections was similarly obtained for the (004) and (100) peaks, shown in Figure S4 in the Supporting Information. For the (004) reflection, we found a single time constant of 4.5 ± 0.75 ps. For the (100) reflection, we determine a time constant of 1.7 ± 0.5 ps for the initial change and of 12 ± 3 ps for the final recovery.

It is worth mentioning that in a single nanotube the excited acoustic modes may generate harmonic oscillations in the measured dynamics. However, the UEC measurements were made here on an ensemble of nanotubes, with somewhat different sizes (diameter ranging between 10 and 20 nm). The resulting transient is thus determined by an incoherent superposition of the displacement field for every nanotube, which is able to preserve the mean atomic displacement along both radial and axial directions but averages out the harmonic oscillations in the transients.

FEELS Experiments. The femtosecond EELS data were recorded in the second-generation ultrafast electron microscope (UEM) at Caltech.[62,63] A train of 220 fs infrared laser pulses (λ = 1038 nm, 500 kHz) was split into two paths; one was frequency-doubled and used to excite the specimen with a fluence of 20 mJ/cm^2, and the other was frequency-tripled into the UV and directed to the photoemissive cathode to generate the electron packets. These pulses were accelerated in the TEM column and dispersed after transmission through the sample in order to provide the energy loss spectrum of the material. The diameter of the converged electron beam (∼200 nm) was sufficiently large to cover a large enough amount of randomly oriented nanotubes. The converging and collection angles were approximately 4 and 7 mrad, respectively.

The preparation of the single-walled nanotubes used in the FEELS experiment is as follows: the nanotubes were dispersed in dimethylformamide under sonication for 15 min. The solution was then drop cast on TEM grids, which were then dried in the vacuum for 24 h. In Figure S2 of the Supporting Information we show the Raman spectrum for the single-walled tubes. Their semiconducting character and the very low amount of defects are evident from the spectrum (see Supporting Information for details).

The EEL spectra were carefully corrected for energy drifts by fitting the zero-loss peak with a Voigt profile. No laser-induced changes in the zero-loss peak beyond ∼1 ps were observed. The transient changes of the bulk plasmon peak were determined by minimizing the differences (χ^2) between an averaged scaled and shifted spectrum before time zero and the respective spectra at each time delay. The resulting fitted scaling factors were close to one for all time delays; the fitted peak shifts are shown in Figure 4c. The time trace was fitted with the combination of an exponential decay and an exponential increase, after convolution with a Gaussian function centered at time zero and full-width-at-half-maximum (fwhm) equal to 0.5 ps, which takes into account the experimental resolution. The time constant for the peak shift is determined to be 0.7 ± 0.2 ps.

Conflict of Interest: The authors declare no competing financial interest.

Supporting Information Available: The Raman spectral characterization of the carbon nanotubes, additional diffraction data, the analytical description of the equilibrium heating model, and further details on the *ab initio* calculations. This material is available free of charge *via* the Internet at http://pubs.acs.org.

Acknowledgment. This work was supported by the National Science Foundation and the Air Force Office of Scientific Research in the Center for Physical Biology at Caltech funded by the Gordon and Betty Moore Foundation. G.M.V. gratefully acknowledge Dr. W. Liang for assistance during UEC experiments. We thank Dr. S. Schäfer, Dr. S. T. Park, Dr. J. Hu for helpful discussions, and Dr. N. Manini for his suggestions and confirmations of the results of the *ab initio* calculations that were performed in this paper.

REFERENCES AND NOTES

1. Li, H. J.; Lu, W. G.; Li, J. J.; Bai, X. D.; Gu, C. Z. Multichannel Ballistic Transport in Multiwall Carbon Nanotubes. *Phys. Rev. Lett.* **2005**, *95*, 086601.
2. Zhou, S. Y.; Siegel, D. A.; Fedorov, A. V.; Lanzara, A. Kohn Anomaly and Interplay of Electron−Electron and Electron−Phonon Interactions in Epitaxial Graphene. *Phys. Rev. B* **2008**, *78*, 193404.
3. Piscanec, S.; Lazzeri, M.; Robertson, J.; Ferrari, A. C.; Mauri, F. Optical Phonons in Carbon Nanotubes: Kohn Anomalies, Peierls Distortions, and Dynamic Effects. *Phys. Rev. B* **2007**, *75*, 035427.
4. Samsonidze, Ge. G.; Barros, E. B.; Saito, R.; Dresselhaus, G.; Dresselhaus, M. S. Electron−Phonon Coupling Mechanism in Two-Dimensional Graphite and Single-Wall Carbon Nanotubes. *Phys. Rev. B* **2007**, *75*, 155420.
5. Noffsinger, J.; Cohen, M. L. Electron−Phonon Coupling and Superconductivity in Double-Walled Carbon Nanotubes. *Phys. Rev. B* **2011**, *83*, 165420.
6. Treacy, M. M. J.; Ebbesen, T. W.; Gibson, J. M. Exceptionally High Young's Modulus Observed for Individual Carbon Nanotubes. *Nature* **1996**, *381*, 678–680.
7. Liang, W. J.; Bockrath, M.; Bozovic, D.; Jason, H.; Hafner, J. H.; Tinkham, M.; Park, H. Fabry−Perot Interference in a Nanotube Electron Waveguide. *Nature* **2001**, *411*, 665–669.
8. Lu, W.; Lieber, C. M. Nanoelectronics from the Bottom Up. *Nat. Mater.* **2007**, *6*, 841–850.
9. Avouris, P.; Chen, Z.; Perebeinos, V. Carbon-Based Electronics. *Nat. Nanotechnol* **2007**, *2*, 605–615.
10. Avouris, P.; Freitag, M.; Perebeinos, V. Carbon-Nanotube Photonics and Optoelectronics. *Nat. Photonics* **2008**, *2*, 341–350.
11. Baloch, K. H.; Voskanian, N.; Bronsgeest, M.; Cumings, J. Remote Joule Heating by a Carbon Nanotube. *Nat. Nanotechnol* **2012**, *7*, 316–319.
12. Park, J.-Y.; Rosenblatt, S.; Yaish, Y.; Sazonova, V.; Ustunel, H.; Braig, S.; Arias, T. A.; Brouwer, P. W.; McEuen, P. L. Electron−Phonon Scattering in Metallic Single-Walled Carbon Nanotubes. *Nano Lett.* **2004**, *4*, 517–520.
13. Zamkov, M.; Woody, N.; Shan, B.; Chang, Z.; Richard, P. Lifetime of Charge Carriers in Multiwalled Nanotubes. *Phys. Rev. Lett.* **2005**, *94*, 056803.
14. Manzoni, C.; Gambetta, A.; Menna, E.; Meneghetti, M.; Lanzani, G.; Cerullo, G. Intersubband Exciton Relaxation Dynamics in Single-Walled Carbon Nanotubes. *Phys. Rev. Lett.* **2005**, *94*, 207401.
15. Gambetta, A.; Manzoni, C.; Menna, E.; Meneghetti, M.; Cerullo, G.; Lanzani, G.; Tretiak, S.; Piryatinski, A.; Saxena, A.; Martin, R. L.; *et al*. Real-Time Observation of Nonlinear Coherent Phonon Dynamics in Single-Walled Carbon Nanotubes. *Nat. Phys.* **2006**, *2*, 515–520.
16. Dyatlova, O. A.; Köhler, C.; Malic, E.; Gomis-Bresco, J.; Maultzsch, J.; Tsagan-Mandzhiev, A. T.; Watermann, T.; Woggon, U. Ultrafast Relaxation Dynamics *via* Acoustic Phonons in Carbon Nanotubes. *Nano Lett.* **2012**, *12*, 2249–2253.
17. Gómez-Navarro, G.; De Pablo, P. J.; Gómez-Herrero, J.; Biel, B.; Garcia-Vidal, F. J.; Rubio, A.; Flores, F. Tuning the Conductance of Single-Walled Carbon Nanotubes by Ion Irradiation in the Anderson Localization Regime. *Nat. Mater.* **2005**, *4*, 534–539.
18. Steiner, M.; Freitag, M.; Perebeinos, V.; Tsang, J. C.; Small, J. P.; Kinoshita, M.; Yuan, D.; Liu, J.; Avouris, P. Phonon Populations and Electrical Power Dissipation in Carbon Nanotube Transistors. *Nat. Nanotechnol* **2009**, *4*, 320–324.
19. Nanot, S.; Haroz, E. H.; Kim, J. H.; Hauge, R. H.; Kono, J. Optoelectronic Properties of Single-Wall Carbon Nanotubes. *Adv. Mater.* **2012**, *24*, 4977–4994.
20. Ajiki, H. Exciton States and Optical Properties of Carbon Nanotubes. *J. Phys.: Condens. Matter* **2012**, *24*, 483001.
21. Chatzakis, I.; Yan, H.; Song, D.; Berciaud, S.; Heinz, T. F. Temperature Dependence of the Anharmonic Decay of Optical Phonons in Carbon Nanotubes and Graphite. *Phys. Rev. B* **2011**, *83*, 205411.
22. Yan, H.; Song, D.; Mak, K. F.; Chatzakis, I.; Maultzsch, J.; Heinz, T. F. Time-Resolved Raman Spectroscopy of Optical Phonons in Graphite. *Phys. Rev. B* **2009**, *80*, 121403(R).
23. Kang, K.; Ozel, T.; Cahill, D. G.; Shim, M. Optical Phonon Lifetimes in Single-Walled Carbon Nanotubes by Time-Resolved Raman Scattering. *Nano Lett.* **2008**, *8*, 4642–4647.
24. Kampfrath, T.; Perfetti, L.; Schapper, F.; Frischkorn, C.; Wolf, M. Strongly Coupled Optical Phonons in the Ultrafast Dynamics of the Electronic Energy and Current Relaxation in Graphite. *Phys. Rev. Lett.* **2005**, *95*, 187403.
25. Cronin, S. B.; Swan, A. K.; Unlü, M. S.; Goldberg, B. B.; Dresselhaus, M. S.; Tinkham, M. Resonant Raman Spectroscopy of Individual Metallic and Semiconducting Single-Wall Carbon Nanotubes Under Uniaxial Strain. *Phys. Rev. B* **2005**, *72*, 035425.
26. *4D Electron Microscopy: Imaging in Space and Time*; Zewail, A. H., Thomas, J. M., Eds.; Imperial College Press: London, 2010.
27. Baum, P.; Yang, D. S.; Zewail, A. H. 4D Visualization of Transitional Structures in Phase Transformations by Electron Diffraction. *Science* **2007**, *318*, 788–792.
28. Yang, D. S.; Lao, C.; Zewail, A. H. 4D Electron Diffraction Reveals Correlated Unidirectional Behavior in Zinc Oxide Nanowires. *Science* **2008**, *321*, 1660–1664.
29. Vanacore, G. M.; Hu, J.; Liang, W.; Bietti, S.; Sanguinetti, S.; Zewail, A. H. Diffraction of Quantum Dots Reveals Nanoscale Ultrafast Energy Localization. *Nano Lett.* **2014**, *14*, 6148–6154.
30. van der Veen, R. M.; Kwon, O. H.; Tissot, A.; Hauser, A.; Zewail, A. H. Single-Nanoparticle Phase Transitions Visualized by Four-Dimensional Electron Microscopy. *Nat. Chem.* **2013**, *5*, 395–402.
31. Schäfer, S.; Liang, W.; Zewail, A. H. Primary Structural Dynamics in Graphite. *New J. Phys.* **2011**, *13*, 063030.
32. Gao, M.; Lu, C.; Jean-Ruel, H.; Lai Chung Liu, L. C.; Alexander Marx, A.; Ken Onda, K.; Shin-ya Koshihara, S.; Yoshiaki Nakano, Y.; Xiangfeng Shao, X.; Takaaki Hiramatsu, T.; *et al*. Mapping Molecular Motions Leading to Charge Delocalization with Ultrabright Electrons. *Nature* **2013**, *496*, 343–346.
33. Clark, J. N.; Beitra, L.; Xiong, G.; Higginbotham, A.; Fritz, D. M.; Lemke, H. T.; Zhu, D.; Chollet, M.; Williams, G. J.; Messerschmidt, M.; *et al.* Ultrafast Three-Dimensional Imaging of Lattice Dynamics in Individual Gold Nanocrystals. *Science* **2013**, *341*, 56–59.
34. Flannigan, D.; Zewail, A. H. Optomechanical and Crystallization Phenomena Visualized with 4D Electron Microscopy: Interfacial Carbon Nanotubes on Silicon Nitride. *Nano Lett.* **2010**, *10*, 1892–1899.
35. Park, S. T.; Flannigan, D.; Zewail, A. H. 4D Electron Microscopy Visualization of Anisotropic Atomic Motions in Carbon Nanotubes. *J. Am. Chem. Soc.* **2012**, *134*, 9146–9149.
36. Maniwa, Y.; Fujiwara, R.; Kira, H.; Tou, H.; Nishibori, E.; Takata, M.; Sakata, M.; Fujiwara, A.; Zhao, X. L.; Iijima, S.; et al. Multiwalled Carbon Nanotubes Grown in Hydrogen Atmosphere: An X-ray Diffraction Study. *Phys. Rev. B* **2001**, *64*, 073105.
37. Xu, G.; Feng, Z.; Popovic, Z.; Lin, J.; Vittal, J. J. Nanotube Structure Revealed by High-Resolution X-ray Diffraction. *Adv. Mater.* **2001**, *13*, 264–267.
38. Lavin, J. G.; Subramoney, S.; Ruoff, R. S.; Berber, S.; Tománek, D. Scroll and Nested Tubes in Multiwall Carbon Nanotubes. *Carbon* **2002**, *40*, 1123–1130.
39. Berber, S.; Tománek, D. Stability Differences and Conversion Mechanism between Nanotubes and Scrolls. *Phys. Rev. B* **2004**, *69*, 233404.
40. Pan, H.; Feng, Y.; Lin, J. Ab Initio Study of Electronic and Optical Properties of Multiwall Carbon Nanotube Structures Made Up of a Single Rolled-Up Graphite Sheet. *Phys. Rev. B* **2005**, *72*, 085415.
41. Chen, B. R.; Trucano, P. Comparisons of Atomic Thermal Motions for Graphite at 300 K Based on X-ray, Neutron, and Phonon-Spectrum Data. *Acta Crystallogr.* **1978**, *A34*, 979–982.

42. Tohei, T.; Kuwabara, A.; Oba, F.; Tanaka, I. Debye Temperature and Stiffness of Carbon and Boron Nitride Polymorphs from First Principles Calculations. *Phys. Rev. B* **2006**, *73*, 064304.
43. Mounet, N.; Marzari, N. First-Principles Determination of the Structural, Vibrational and Thermodynamic Properties of Diamond, Graphite, and Derivatives. *Phys. Rev. B* **2005**, *71*, 205214.
44. Jiang, J.-W.; Wang, J.-S.; Li, B. Thermal Expansion in Single-Walled Carbon Nanotubes and Graphene: Nonequilibrium Green's Function Approach. *Phys. Rev. B* **2009**, *80*, 205429.
45. Lazzeri, M.; Mauri, F. Coupled Dynamics of Electrons and Phonons in Metallic Nanotubes: Current Saturation from Hot-Phonon Generation. *Phys. Rev. B* **2006**, *73*, 165419.
46. Hirtschulz, M.; Malic, E.; Milde, F.; Knorr, A. Excitation-Induced Dephasing and Ultrafast Intrasubband Relaxation in Carbon Nanotubes. *Phys. Rev. B* **2009**, *80*, 085405.
47. Bonini, N.; Lazzeri, M.; Marzari, N.; Mauri, F. Phonon Anharmonicities in Graphite and Graphene. *Phys. Rev. Lett.* **2007**, *99*, 176802.
48. *Comprehensive Nanoscience and Nanotechnology*; Lanzani, G.; Lüer, L. Carbon Nanotubes: Electronic Structure and Spectroscopy. Eds.; Academic Press: 2010.
49. Köler, C.; Watermann, T.; Knorr, A.; Malic, E. Microscopic Study of Temporally Resolved Carrier Relaxation in Carbon Nanotubes. *Phys. Rev. B* **2011**, *84*, 153407.
50. Nixon, D. E.; Parry, G. S. The Expansion of the Carbon–Carbon Bond Length in Potassium Graphites. *J. Phys. C* **1969**, *2*, 1732.
51. Chan, C. T.; Kamitakahara, W. A.; Ho, K. M. Charge-Transfer Effects in Graphite Intercalates: Ab Initio Calculations and Neutron-Diffraction Experiment. *Phys. Rev. Lett.* **1987**, *58*, 1528–1531.
52. Aizawa, T.; Souda, R.; Otani, S.; Ishizawa, Y.; Oshima, C. Anomalous Bond of Monolayer Graphite on Transition-Metal Carbide Surfaces. *Phys. Rev. Lett.* **1990**, *64*, 768–771.
53. Börrnert, F.; Barreiro, A.; Wolf, D.; Katsnelson, M. I.; Büchner, B.; Vardersypen, L. M. K.; Rümmeli, M. Lattice Expansion in Seamless Bilayer Graphene Constrictions at High Bias. *Nano Lett.* **2012**, *12*, 4455–4459.
54. Dumitrică, T.; Garcia, M. E.; Jeschke, H. O.; Yakobson, B. I. Breathing Coherent Phonons and Caps Fragmentation in Carbon Nanotubes Following Ultrafast Laser Pulses. *Phys. Rev. B* **2006**, *74*, 193406.
55. Wang, F.; Dukovic, G.; Brus, L. E.; Heinz, T. F. Time-Resolved Fluorescence of Carbon Nanotubes and Its Implication for Radiative Lifetimes. *Phys. Rev. Lett.* **2004**, *92*, 177401.
56. Felten, A.; Gillon, X.; Gulas, M.; Pireaux, J. J.; Ke, X.; Van Tendeloo, G.; Bittencourt, C.; Najafi, E.; Hitchcock, A. P. Measuring Point Defect Density in Individual Carbon Nanotubes Using Polarization-Dependent X-ray Microscopy. *ACS Nano* **2010**, *4*, 4431–4436.
57. Najafi, E.; Wang, J.; Hitchcock, A. P.; Guan, J.; Dénommée, S.; Simard, B. Characterization of Single-Walled Carbon Nanotubes by Scanning Transmission X-ray Spectromicroscopy: Purification, Order and Dodecyl Functionalization. *J. Am. Chem. Soc.* **2010**, *132*, 9020–9029.
58. Zhou, S. Y.; Gweon, G.-H.; Graf, J.; Fedorov, A. V.; Spataru, C. D.; Diehl, R. D.; Kopelevich, Y.; Lee, D.-H.; Louie, S. G.; Lanzara, A. First Direct Observation of Dirac Fermions in Graphite. *Nat. Phys.* **2006**, *2*, 595–599.
59. Ostojic, G. N.; Zaric, S.; Kono, J.; Strano, M. S.; Moore, V. C.; Hauge, R. H.; Smalley, R. E. Interband Recombination Dynamics in Resonantly Excited Single-Walled Carbon Nanotubes. *Phys. Rev. Lett.* **2004**, *92*, 117402.
60. Gokus, T.; Hartschuh, A.; Harutyunyan, H.; Allegrini, M.; Hennrich, F.; Kappes, M.; Green, A. A.; Hersam, M. C.; Araújo, P. T.; Jorio, A. Exciton Decay Dynamics in Individual Carbon Nanotubes at Room Temperature. *Appl. Phys. Lett.* **2008**, *92*, 153116.
61. George, P. A.; Strait, J.; Dawlaty, J.; Shivaraman, S.; Chandrashekhar, M.; Rana, F.; Spencer, M. G. Ultrafast Optical-Pump Terahertz-Probe Spectroscopy of the Carrier Relaxation and Recombination Dynamics in Epitaxial Graphene. *Nano Lett.* **2008**, *8*, 4248–4251.
62. Carbone, F.; Kwon, O.-H.; Zewail, A. H. Dynamics of Chemical Bonding Mapped by Energy-Resolved 4D Electron Microscopy. *Science* **2009**, *325*, 181–184.
63. Carbone, F.; Barwick, B.; Kwon, O.-H.; Park, H. S.; Spencer, J. B.; Zewail, A. H. EELS Femtosecond Resolved in 4D Ultrafast Electron Microscopy. *Chem. Phys. Lett.* **2009**, *468*, 107–111.
64. Stéphan, O.; Taverna, D.; Kociak, M.; Suenaga, K.; Henrard, L.; Colliex, C. Dielectric Response of Isolated Carbon Nanotubes Investigated by Spatially Resolved Electron Energy-Loss Spectroscopy: From Multiwalled to Single-Walled Nanotubes. *Phys. Rev. B* **2002**, *66*, 155422.
65. Knupfer, M.; Pichler, T.; Golden, M. S.; Fink, J.; Rinzler, A.; Smalley, R. E. Electron Energy-Loss Spectroscopy Studies of Single Wall Carbon Nanotubes. *Carbon* **1999**, *37*, 733–738.
66. Reed, B. W.; Sarikaya, M. Electronic Properties of Carbon Nanotubes by Transmission Electron Energy-Loss Spectroscopy. *Phys. Rev. B* **2001**, *64*, 195404.
67. Barwick, B.; Flannigan, D. J.; Zewail, A. H. Photon-Induced near-Field Electron Microscopy. *Nature* **2009**, *462*, 902–906.
68. Rossouw, D.; Bugnet, M.; Botton, G. A. Structural and Electronic Distortions in Individual Carbon Nanotubes under Laser Irradiation in the Electron Microscope. *Phys. Rev. B* **2013**, *87*, 125403.
69. Gonze, X.; Amadon, B.; Anglade, P.-M.; Beuken, J.-M.; Bottin, F.; Boulanger, P.; Bruneval, F.; Caliste, D.; Caracas, R.; Côté, M.; et al. ABINIT: First-Principles Approach to Material and Nanosystem Properties. *Comput. Phys. Commun.* **2009**, *180*, 2582–2615.
70. Schafer, S.; Liang, W.; Zewail, A. H. Structural Dynamics of Surfaces by Ultrafast Electron Crystallography: Experimental and Multiple Scattering Theory. *J. Chem. Phys.* **2011**, *135*, 214201.
71. Kumar, M.; Ando, Y. Chemical Vapor Deposition of Carbon Nanotubes: A Review on Growth Mechanism and Mass Production. *J. Nanosci. Nanotechnol.* **2010**, *10*, 3739–3758.
72. Schäfer, S.; Liang, W.; Zewail, A. H. Structural Dynamics and Transient Electric-Field Effects in Ultrafast Electron Diffraction from Surfaces. *Chem. Phys. Lett.* **2010**, *493*, 11–18.
73. Yang, D.; Frindt, R. F. Powder X-ray Diffraction of Two-Dimensional Materials. *J. Appl. Phys.* **1996**, *79*, 2376.
74. Warren, B. E. X-ray Diffraction in Random Layer Lattices. *Phys. Rev.* **1941**, *59*, 693–698.